Efficient Activation of H_2O_2 by C_{60}/MIL-101(Fe,Cu) Composite for Degradation of Methylene Blue under Visible Light

Zhuyou Zhou · Yufeng Ji · Yong Wang · Menghe Liu · Ying Xu · Ruijie Liu · Mingjie Yang · Congyang Zou

Abstract In this study, the carbon-doped bimetallic organic framework C_{60}/MIL-101(Fe,Cu) catalyst was prepared for the first time via solvothermal synthesis method. The catalysts were characterized using X-ray diffraction (XRD), Fourier transform infrared spectroscopy (FT-IR), and a series of other instruments. At the same time, methylene blue (MB) was used as the target degradation material to investigate the catalytic performance of H_2O_2 for MB degradation under visible light. The degradation experiment showed that the removal rate of C_{60}/MIL-101(Fe,Cu) to MB reached 99.2% within 80 min. Furthermore, cyclic experiments demonstrated good stability and reusability of the catalyst. Finally, the degradation mechanism of the reaction was deduced by quenching experiment, UV–vis diffuse reflection and mott-Schottky plots. The results show that hydroxyl radical (·OH) and superoxide radical (·O_2^-) play a major role in the degradation of MB during photo-Fenton process.

Z. Zhou · Y. Ji · Y. Wang · M. Liu · Y. Xu · R. Liu ·
M. Yang · C. Zou (✉)
School of Environmental Science and Engineering, Suzhou University of Science and Technology, Suzhou 215009, Jiangsu, China
e-mail: ericcongyang@126.com

Z. Zhou
e-mail: zhouzhuyou2021@163.com

Y. Ji
e-mail: 934579643@qq.com

1 Introduction

Printing and dyeing wastewater had the characteristics of large amount of water, high content of organic toxicants, complex composition and difficult degradation (Lu et al., 2023). Methylene blue, as a kind of azo dye, was widely used in printing and dyeing, manufacturing and other industries (Chavan et al., 2023; Li et al., 2020). Because its aromatic structure was not easy to be destroyed, it was difficult to degrade by traditional methods such as biochemical and chemical oxidation (Li et al., 2018; Tayeb et al., 2023). Therefore, modern enterprises urgently need an efficient and environmentally friendly technology to degrade printing and dyeing wastewater.

Advanced oxidation processes (AOPs) were the use of light, electricity, catalysis and other technologies, through physical and chemical processes to catalyze the production of a large number of strong oxidizing free radicals (such as hydroxyl radicals (·OH), superoxide radicals (·O_2^-)) (Chen et al., 2022; Pestana et al., 2023). Due to its ability to degrade and mineralize such insoluble organic compounds had aroused great interest. Fenton system was one of the most representative advanced oxidation technologies, which had the advantages

of high treatment efficiency and relatively low cost. However, Fenton system had several serious disadvantages, such as a narrow operating pH range (2–4) and a large consumption of H_2O_2 during application (Lu et al., 2022; Zhang et al., 2022). Photocatalytic technology was not prone to secondary pollution in the degradation process. In order to better overcome Fenton process's disadvantages, many studies had introduced photocatalysis technology into the collaborative degradation of pollutants. For instance, Xu et al. had synthesized $FeTiO_3$/g-C_3N_4 nanoparticle photocatalyst with much higher catalytic activity than pure $FeTiO_3$ and pure g-C_3N_4 in the degradation of TCH under visible light (Xu et al., 2022). Gu et al. had successfully prepared magnetic metal-organogels (MMOG) by in-situ reaction of MOG and ferric oxide, and used this catalyst to degrade Rhb efficiently over a wide pH range (Gu et al., 2022). The Ag_2S/MIL-53(Fe) heterojunction composites prepared by Deng et al. showed stronger photocatalytic activity than pure MIL-53(Fe) and pure Ag_2S. In addition, due to the synergistic effect of photocatalysis and Fenton catalysis, the addition of H_2O_2 can further improve the degradation efficiency (Deng et al., 2020). Therefore, it was particularly important to prepare efficient iron matrix composites for photo-Fenton degradation of organic dyes.

Fe-based organic frame materials (Fe-MOFs) were porous materials composed of iron ions or iron clusters self-assembled with organic ligands (Wan et al., 2020). Fe-MOFs had the advantages of unique structure, excellent performance, large specific surface area, abundant nanocavity, adjustable porosity and open pore, etc., which helped to fully expose the reaction site and accelerate electron transfer. In Fenton-like catalysts, the slow transition from Fe^{3+} to Fe^{2+} hinders their catalytic activity (Du et al., 2022; Tao et al., 2021; Yang et al., 2021). As a widely available metal, copper had been added to catalysts to enhance their activity as an accelerator. In addition, MOFs had good structural adjustability, and the conversion rate of Fe^{3+} to Fe^{2+} in MOFs can be accelerated by adding Cu^{2+}. Similar to the conversion of Fe^{3+} to Fe^{2+}, Cu^{2+} to Cu^+ cycling can also activate H_2O_2 to produce ·OH. Thus, the heterogeneous catalytic degradation efficiency of H_2O_2 pollutants can be improved (Feng et al., 2023). Liang H et al. successfully synthesized CUMSs/MIL-101(Fe,Cu) by solvothermal

method. Compared with conventional MIL-101(Fe), CUMSs/MIL-101(Fe,Cu) was 20 times more effective at neutral-pH degradation of ciprofloxacin (CIP). It had been proved that the thermodynamic favorable reaction of Cu^+ with Fe^{3+} and π-cation interactions accelerates the redox cycle of Cu^+/Cu^{2+} CUMSs and Fe^{3+}/Fe^{2+} CUMSs. Therefore, MIL-101(Fe) was combined with other metals to construct coordination unsaturated metal sites, which promoted the conversion of Fe^{3+} to Fe^{2+}, and was an important way to improve the Fenton reaction rate (Liang et al., 2021).

Semiconductor composite MOFs photocatalytic materials were also a research hotspot in recent years. At present, the most studied semiconductor materials mainly included TiO_2, Graphene (GO), V_2O_5 and g-C_3N_4 (Hui et al., 2022; Hussain et al., 2022; Shaheen et al., 2023). For example, Lin J et al. prepared GO@MIL-101(Fe) composites by hydrothermal method. On this basis, a visible light/GO@MOF/H_2O_2 photocatalytic system was developed for the degradation of tris (2-chloroethyl) phosphate (TCEP). Under visible light irradiation, 15%GO@MIL-101(Fe) photo-Fenton degraded TCEP about twice as efficiently as MIL-101(Fe). This was due to the high electrical conductivity and good photoresponsiveness of graphene oxide, which enabled rapid activation and electron transfer (Lin et al., 2020). Zhu et al. had successfully fabricated E-spun g-C_3N_5/MIL-101(Fe)/PANCMA NFs via the electrospinning of g-C_3N_5/MIL-101(Fe) and PANCMA solution. The photocatalyst can effectively degrade drug contaminants such as carbamazepine, ciprofloxacin and tetracycline (Zhu et al., 2022). These results showed that carbon nanocomposites were suitable for photocatalytic degradation of pollutants (Lin et al., 2023). According to literature search, we found that fullerenes (C_{60}) had better photocatalytic ability than GO, but there were few reports on the preparation of C_{60}-doped MOF composites and its application in dye degradation.

In this study, the synthesis process of MIL-101(Fe) was used as the template, and Cu and C_{60} were doped successively. By doping Cu, the conversion of Fe^{3+} and Fe^{2+} can be promoted to produce more ·OH (Guo et al., 2020). By doping C_{60}, the absorption of the material in the visible region can be improved, and the rapid recombination of photogenerated e^-/h^+ can be inhibited (Watariguchi et al., 2014). Finally, the photo-Fenton degradation ability of the composite material was greatly improved. Based on this, the main

research contents of this paper included the following aspects: (1)C_{60}/MIL-101(Fe,Cu) composite catalyst was prepared by one-step solvothermal method, and the corresponding material characterization was carried out; (2)Using methylene blue (MB) as the model pollutant, the photo-Fenton degradability was analyzed under different initial pH, H_2O_2 concentration and catalyst dosage, and the reusability and stability of the catalyst are evaluated. (3)The main possible reaction mechanisms were proposed by optical, electrochemical and electron spin resonance techniques.

2 Materials and Methods

2.1 Materials

Crystalline fullerene powder (99.9% purity) was purchased from Suzhou Dade Carbon Nanotechnology Co., Ltd. Copper nitrate trihydrate ($Cu(NO_3)_2 \cdot 3H_2O$), ferric chloride ($FeCl_3 \cdot 6H_2O$), terephthalic acid (H_2BDC), N, N-dimethylformamide (DMF), absolute ethyl alcohol (CH_3CH_2OH), H_2O_2 (30%, W/W), sulphuric acid (H_2SO_4), sodium hydroxide (NaOH), isopropyl alcohol (IPA), trichloromethane ($CHCl_3$) and L-histidine were purchased from Aladdin Reagent Co., Ltd (Shanghai,China). Methylene blue (MB) was used as model dye pollutants without further purification. Deionized (DI) water was used for all the solutions configured in the experiments.

2.2 Catalyst Characterizations

Power X-ray diffraction (XRD) analysis on a D8 Advance diffrac-tometer (Bruker, Germany) was performed to identify the structure and crystallinity of the as-prepared samples with monochromatic high-intensity Cu Kα radiation ($\lambda = 1.5406$ Å). The specific surface area and pore size distribution of all samples were determined by using Brunauer–Emmett–Teller (BET) method, respectively, based on the adsorption data of N_2 adsorption–desorption isotherms collected at 77 K on a NOVA4000 analyzer. Scanning electronic microscopy (SEM; JEOL, Japan) images were acquired on Quanta FEG 250 field emission scanning electron microscope equipped with energy dispersive spectrometer (EDS). Fourier transform infrared (FT-IR) spec-troscopy (Nicolet6700; Thermo Ltd., Japan) was carried out to detect the chemical bonds on the surface of the catalyst. UV–vis diffuse reflectance spectra (UV–vis DRS) were obtained by UV–vis spectrophotometer (UV-3600, Shimadzu Ltd., Japan). X-ray photoelectro spectroscopy (XPS; XSAM 800) was employed to characterize the elemental states. Zeta potentials and average particle size of materials were measured by a zeta potentiometer (Nano-ZS90, Malvern, UK). Electron paramagnetic resonance (EPR; Bruker, Germany) can be used to measure the free radicals produced by materials in different systems. The sample was analyzed by thermogravimetry (TG) on the NETZSCH TG 209 F1 instrument, and the temperature ranged from room temperature to 800℃ with the rising rate of $20° \cdot min^{-1}$.

2.3 Preparation of Catalyst

As shown in Fig. 1, 7.5 mmol $FeCl_3 \cdot 6H_2O$、2.5 mmol $Cu(NO_3)_2 \cdot 3H_2O$ and 5.0 mmol H_2BDC was respectively dispersed in 15 mL DMF and sonicated for 15 min, and then $FeCl_3 \cdot 6H_2O$ solution was mixed
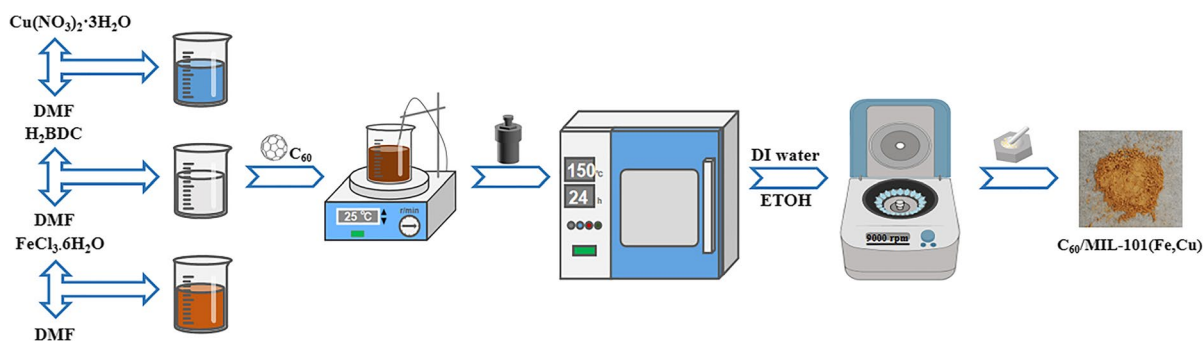
Fig. 1 Preparation process of C_{60}/MIL-101(Fe,Cu) material

with the H_2BDC solution under ultrasonic conditions, and C_{60} were added at the same time to obtain the yellow precursor solution. The mixed solution was then transferred to a 100 mL Teflon-lined steel autoclave and reacted at 150℃ for 24 h. After the reaction, the precipitates were centrifuged and washed with water and ethanol for several times. Finally, the precipitates were dried at 60℃ for 10 h to obtain brown C_{60}/MIL-101(Fe,Cu) materials. For comparison, MIL-101(Fe,Cu) material was synthesized without adding C_{60} according to the above experimental procedure.

2.4 Photo-Fenton Degradation

In this work, a 300 W ultraviolet visible light lamp (OSRAM, Germany) with a 400 nm cut-off filter was used as the light source, and the distance between the lamp and the reactor was about 10 cm. In general, a certain amount of catalyst was dispersed in 50 mL contaminants aqueous solution (20 mg/L) in the reactor. Before illumination, the reactor wall was wrapped with tinfoil and stirred in darkness for 30 min to achieve adsorption equilibrium. Then, a certain concentration of H_2O_2 was added to the suspension. After that, 3 mL of suspension was taken out with a syringe every 20 min and filtered with 0.22 µm filter membrane, and then the residual concentration of contaminant was determined by ultraviolet visible spectrophotometer (Mapada P1, Shanghai,China).

According to the strong absorption peak of MB at 664 nm, the degradation effect of MB was measured, and the removal rate was calculated by the following equation:

$$Removal rate(\%) = \left(1 - C/C_0\right) \times 100\% \qquad (1)$$

where C_0 and C represent the concentrations of contaminant in the initial solution and that at time t, respectively. The standard curve of MB was shown in Fig. S1.

The effects of catalyst dosage, initial pH (adjusted with 0.1 mol/L HCl and NaOH), H_2O_2 concentration and different water samples on the photocatalytic degradation efficiency were evaluated under visible light irradiation. Meanwhile, the cyclability and stability were evaluated by six consecutive reuse experiments and infrared spectral characterization.

3 Results and Discussion

3.1 Surface Morphology

SEM images of MIL-101(Fe), MIL-101(Fe,Cu) and C_{60}/MIL-101(Fe,Cu) were shown in Fig. 2. MIL-101(Fe) had a distinct angular octahedral structure, while MIL-101(Fe,Cu) had great differences in morphology. Comparing Fig. 2a-b, it can be seen that the octahedral structure becomes spindle shaped after Cu doping. This was mainly due to the introduction of the Cu ions interferes with the coordination of carboxyl groups in Fe^{3+} and H_2BDC, which in turn affects the growth of grains (Wu et al., 2021). Table 1 showed the EDS mapping analysis results corresponding to MIL-101(Fe,Cu). Obviously, the Cu content of the catalyst was much lower than the preset Cu doping amount, which may be because Fe and H_2BDC had a very strong coordination ability, so the coordination ability of Cu and H_2BDC was obviously weak (Cen et al., 2020; Khosravi et al., 2022). Compared with MIL-101(Fe,Cu), the average particle size of C_{60}/MIL-101(Fe,Cu) was larger and still maintains the spindle morphology. As shown in Fig. 2c, the fine spherical particles on the surface of C_{60}/MIL-101(Fe) were C_{60} clusters, while the mass ratio of C element in C_{60}/MIL-101(Fe,Cu) was higher than that of MIL-101(Fe,Cu) due to C_{60} doping. The results showed that the C_{60}/MIL-101(Fe,Cu) composites synthesized by one-step solvothermal synthesis had high purity and tight interfacial bonding.

The chemical composition and oxidation state of C_{60}/MIL-101(Fe,Cu) were investigated by XPS analysis (Fig. 3). The XPS survey (Fig. 3a) showed the expected characteristic peaks of Fe 2p, Cu 2p, C 1 s and O 1 s (Ding et al., 2021). This phenomenon, together with EDS analysis, confirmed the surface elements composition of C_{60}/MIL-101(Fe,Cu). To further confirm the valence states of metallic elements, we analyzed the XPS spectrum of Fe 2p and Cu 2p. As shown in Fig. 3c, the binding energies of Fe 2$p_{3/2}$ and Fe 2$p_{1/2}$ were located at 710.92 and 724.13 eV (Xiong et al., 2021). In addition, there was an obvious characteristic satellite peak at about 719.13 eV, which was considered to be the characteristic peak of Fe^{3+}. In the Cu 2p region (Fig. 3b), Cu 2$p_{3/2}$ and Cu 2$p_{1/2}$ showed two characteristic peaks at 933.2 and 953.0 eV, respectively, corresponding to the characteristic peaks of Cu^{2+} species. In addition,
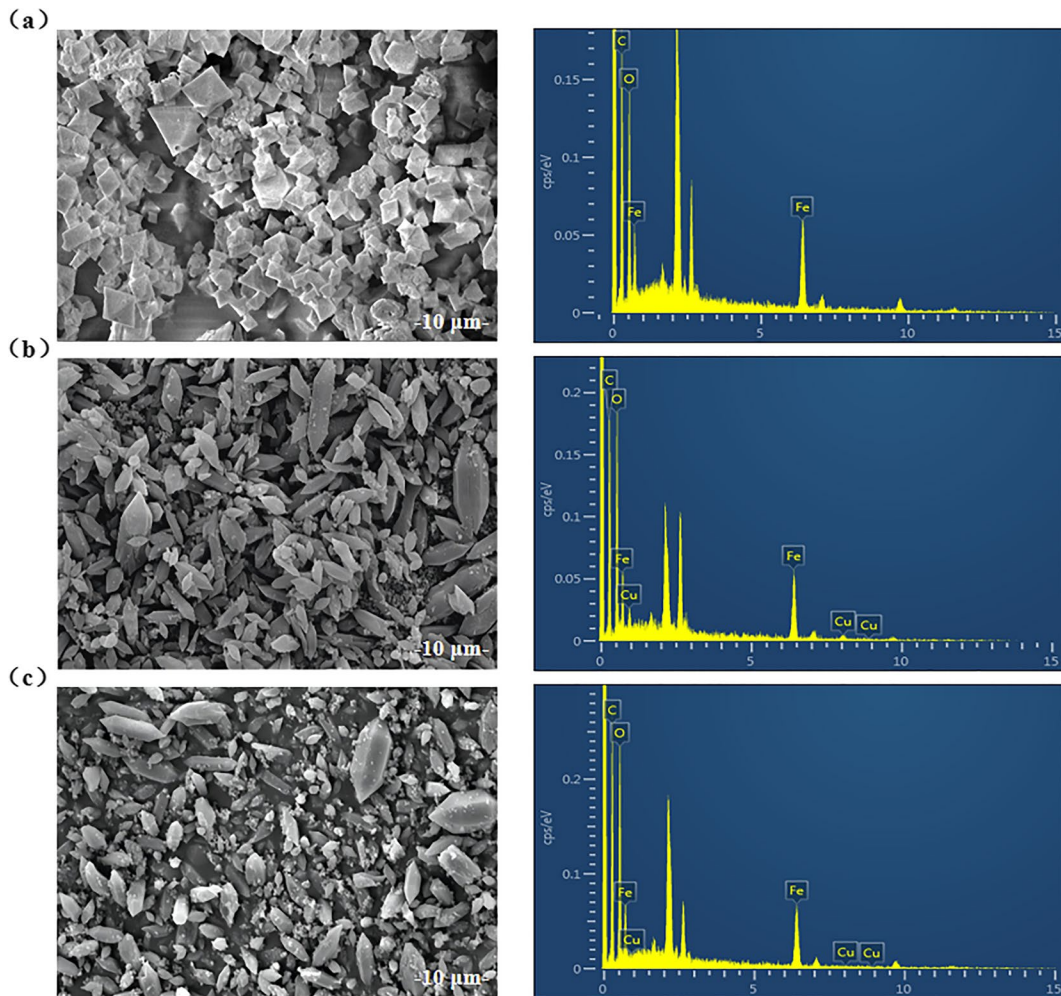
Fig. 2 SEM–EDS images of (**a**) MIL-101(Fe), (**b**) MIL-101(Fe,Cu); (**c**) C_{60}/MIL-101(Fe,Cu)

Table 1 EDS weight and mean particle size of different materials

| Samples	Fe Wt%	Cu Wt%	C Wt%	O Wt%	mean particle size (nm)
MIL-101(Fe)	26.6	0	43.2	30.2	716.4
MIL-101(Fe,Cu)	21.1	4.1	39.2	35.6	781.9
C_{60}/MIL-101(Fe,Cu)	20.5	3.6	42.1	33.8	841.2

three wobbly satellite peaks of Cu 2*p* appeared in the 930 eV to 960 eV range, further indicating that copper exists primarily on the surface of the composite in the form of Cu^{2+} (Ansari et al., 2019). These analysis results would have great significance for the explanation of degradation mechanism.

3.2 XRD and FT-IR Characterizations

The crystal compositions of C_{60}, MIL-101(Fe), MIL-101(Fe,Cu) and C_{60}/MIL-101(Fe,Cu) had been investigated, and the corresponding XRD patterns were shown in Fig. 4a. The diffraction peaks of
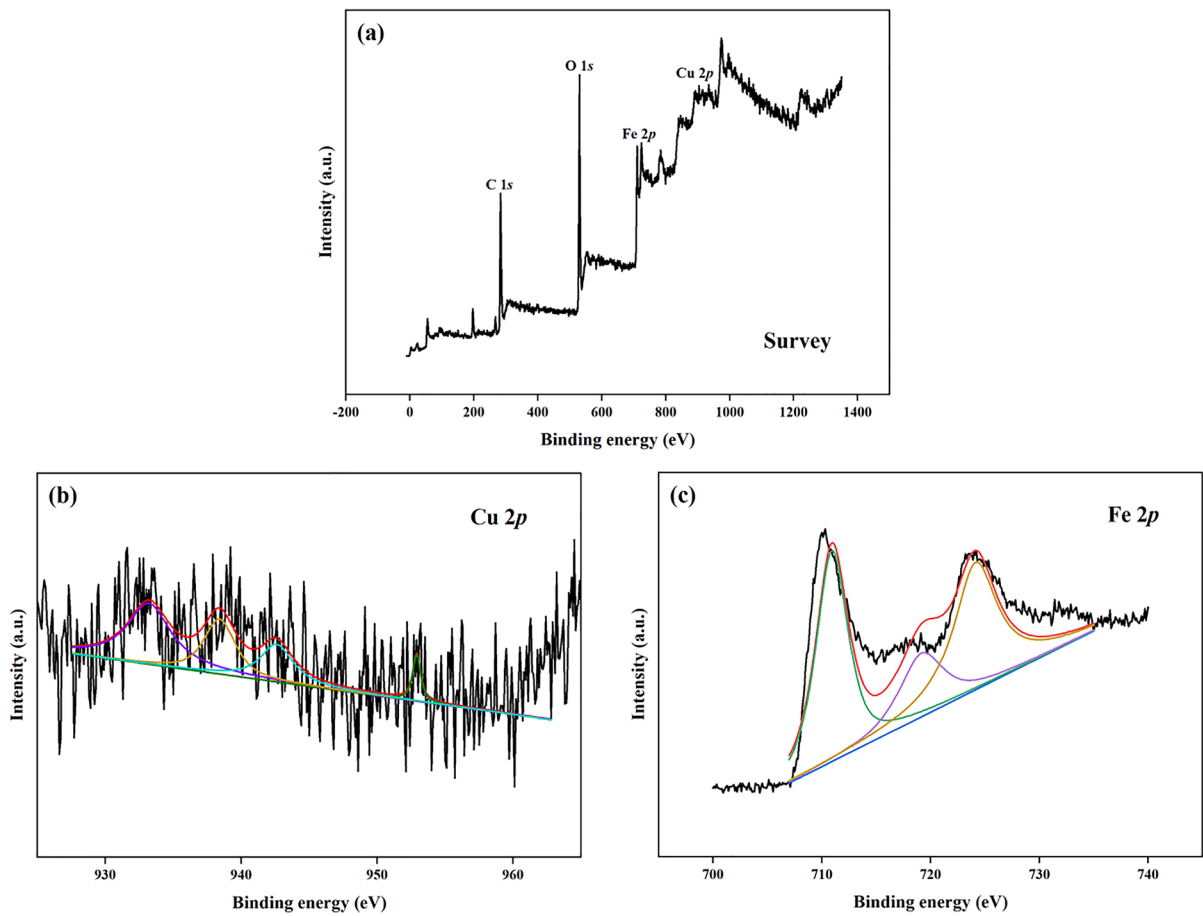
Fig. 3 The XPS spectra of C_{60}/MIL-101(Fe,Cu); (**a**) survey spectra, (**b**) Cu 2*p*, (**c**) Fe 2*p*
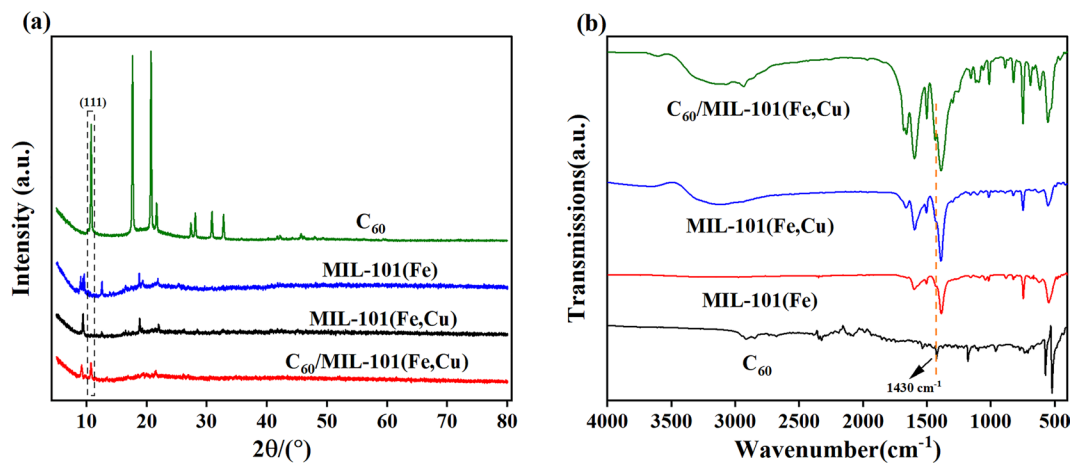
Fig. 4 XRD patterns (**a**) and FT-IR spectra (**b**) of different materials

MIL-101(Fe) were located at $2\theta = 9.58°$, $18.8°$ and $21.8°$, corresponding to (311), (511) and (852) crystal planes, respectively, which were consistent with those reported in the literature (Li et al., 2017). Compared with MIL-101(Fe), the peak position of MIL-101(Fe,Cu) did not change, but the peak intensity was slightly enhanced. The may be due to a small amount of Cu^{2+} competing with Fe^{3+} for coordination resulting in a change in peak intensity. The characteristic peak of (111) crystal facet of C_{60} was found in C_{60}/MIL-101(Fe,Cu) composites, which indicated its successful doping into MIL-101(Fe,Cu) material (Chen et al., 2019). In addition, the positions of the characteristic peaks belonging to MIL-101(Fe,Cu) did not change in the C_{60}/MIL-101(Fe,Cu) composites, suggesting that the introduction of C_{60} did not disrupt the crystalline structure of the MOFs during the synthesis process (Dhankhar et al., 2016). The results showed that C_{60}/MIL-101(Fe,Cu) was successfully prepared by one-step solvothermal method.

The functional groups on the surface of materials can be understood by infrared spectroscopy. It can be seen from Fig. 4b that the characteristic peaks of MIL-101(Fe), MIL-101(Fe,Cu) and C_{60}/MIL-101(Fe,Cu) were very similar, appearing at 546, 747.7, 1017.4, 1389.4 and 1601 cm^{-1}, corresponding to the stretching vibration of the Fe–O bond, the out of plane bending vibration of C-H of benzene ring, the stretching vibration of C-O–O band and the symmetric and asymmetric vibrations of carboxyl group, which was basically consistent with literature reports. But there was also a slight difference at 1601 cm^{-1}. Among them, 1601 cm^{-1} belonged to the asymmetric vibration of COO- in the organic ligand. This may be due to the difference caused by the small amount of Cu^{2+} coordinating with H_2BDC (Shah et al., 2023). At the same time, this study found that the organic skeleton of the composite did not collapse after adding C_{60}. The characteristic peak of C_{60} appeared in C_{60}/MIL-101(Fe,Cu) at 1430 cm^{-1} (Granados-Tavera et al., 2023).

3.3 Bet analysis

Figure 5a showed the results of nitrogen adsorption/desorption isotherms of different catalysts. As can be seen from Fig. 5a, the MIL-101(Fe) exhibited a typical type IV desorption curve with a type H4 hysteresis ring, while MIL-101(Fe,Cu) and C_{60}/

MIL-101(Fe,Cu) exhibited typical type I desorption curves. This indicated that the mesoporous structure of the composite was changed after Cu atom doping. Table 2 also displayed the specific surface area, pore volume and pore size of the samples. MIL-101(Fe,Cu) had a lower specific surface area and smaller pore volume as compared to pure MIL-101(Fe), suggesting that the addition of organomemetal atoms (Cu^{2+}) did indeed block the pores and changed the morphology and structure of MIL-101(Fe). Conversely, the increase in pore size indicated that the surface of MIL-101(Fe) partially formed copper species (Duan et al., 2018).

3.4 Zeta Potential and Contact Angle Measurements

Figure 5b was the zeta potential diagram of the samples at different pH values. When the pH was low, the surface of the adsorbent was positively charged, and the adsorption performance of the adsorbent on MB was enhanced due to the electronegativity of methylene blue solution. Meanwhile, the adsorption efficiency of MB decreased with increasing pH, which was attributed to the large amount of OH^- in the alkaline solution competing with MB for adsorption sites and inhibiting the adsorption process (Aliannezhadi et al., 2023). Water contact angle tests of different materials were employed to further demonstrate the hydrophilic properties of the materials. It could be seen that C_{60}/MIL-101(Fe,Cu) had the strongest hydrophilic property, followed by MIL-101(Fe,Cu) and MIL-101(Fe). The water contact Angle of C_{60}/MIL-101 (Fe,Cu) was 0° within 2 s, which indicated that the material had excellent hydrophilicity (Zhang et al., 2020). From the above analysis, it can be seen that C_{60}/MIL-101(Fe,Cu) had the most positive potential in different pH solutions. At the same time, C_{60}/MIL-101(Fe,Cu) had the strongest hydrophilic properties. Therefore, C_{60}/MIL-101(Fe,Cu) was more likely to adsorb pollutants to its surface for catalytic degradation.

3.5 Electrochemical Characterizations

In order to understand the photocatalytic ability of the materials, the photoelectric properties of the materials were characterized. The charge transfer efficiency of the materia was investigated using EIS. It can be seen from Fig. 6a that the arc radius of C_{60}/
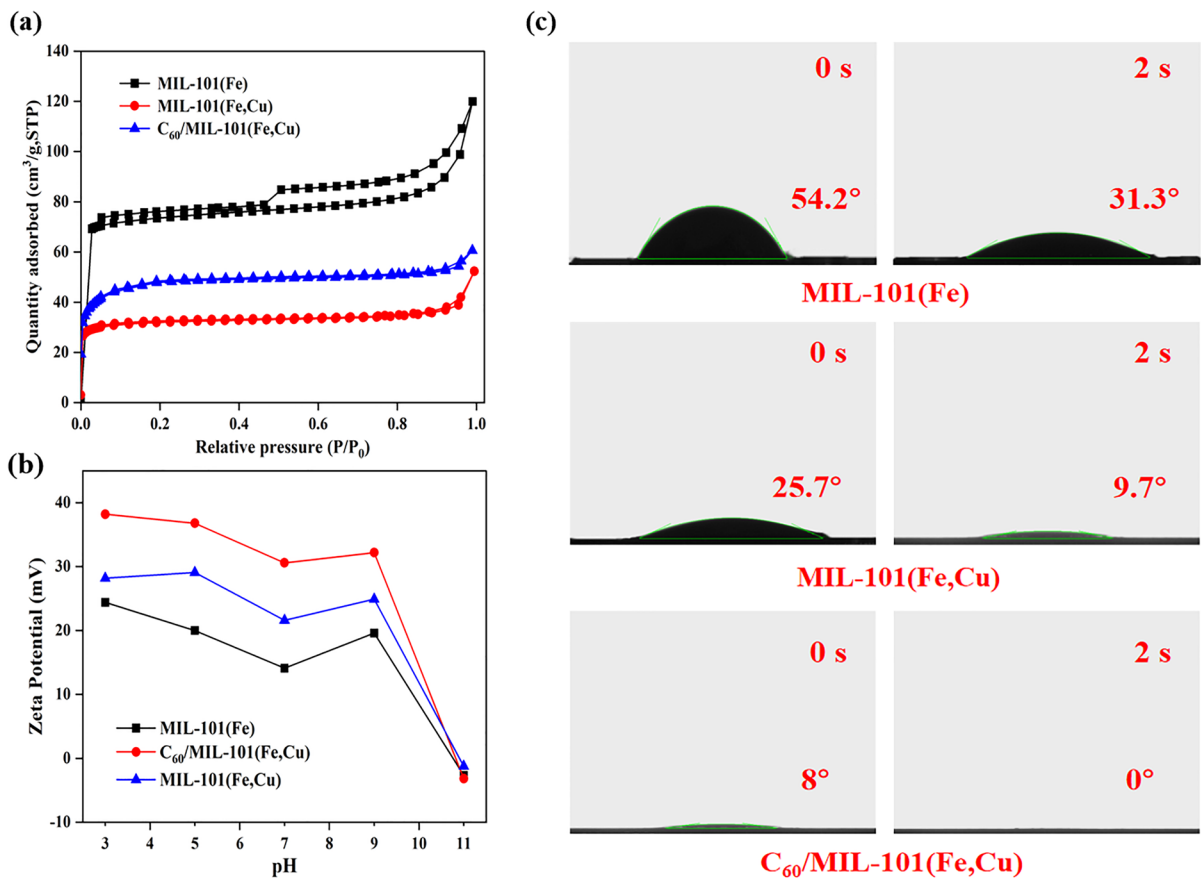
Fig. 5 N$_2$ adsorption–desorption isotherms (**a**), Zeta potential (**b**) and water contact Angle (**c**) of different materials

Table 2 Pore structure parameters of different materials

Sample	S$_{BET}$ (m^2 g^{-1})	Pore volume (cm^3 g^{-1})	Pore size (nm)
MIL-101(Fe)	225.7777	0.185502	3.2865
MIL-101(Fe,Cu)	95.6362	0.080944	3.3855
C$_{60}$/MIL-101(Fe,Cu)	144.7598	0.093849	2.5932

MIL-101(Fe,Cu) was smaller than that of pure MIL-101(Fe,Cu). As the radius of the EIS diagram was smaller, the resistance was also smaller. EIS results showed that C$_{60}$/MIL-101(Fe,Cu) had better charge transfer efficiency. Figure 6b demonstrated the transient photocurrent response of different materials under light. Compared with pure MIL-101(Fe,Cu), the doping of C$_{60}$ can make the MOFs material had a stronger photocurrent (Sharma et al., 2023). The

results showed that more photogenerated electrons can be produced and electrons can be effectively transferred on the composite material. C$_{60}$/MIL-101(Fe,Cu) exhibited better photocatalytic activity than pure MIL-101(Fe,Cu) because of the efficient separation and transfer of charge on the material (Feizpoor et al., 2023).

3.6 Effects of Parameters on the Degradation of MB

3.6.1 Effect of Different Catalytic Systems

Figure 7a showed the photocatalytic degradation of MB by different material systems. Under the dark condition, C$_{60}$/MIL-101(Fe,Cu) adsorbed MB and reached the adsorption–desorption equilibrium after 30 min. Meanwhile, C$_{60}$/MIL-101(Fe,Cu) showed higher photo-Fenton-degradation than MIL-101(Fe) and MIL-101(Fe,Cu) under visible light and H$_2$O$_2$,
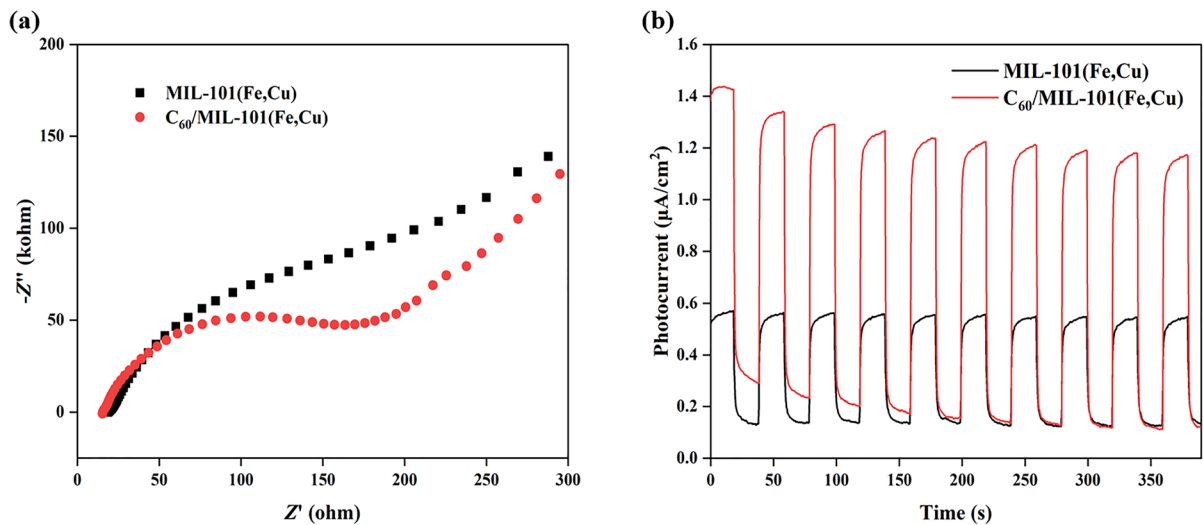
Fig. 6 Photocurrent response (**a**) and EIS Nyquist (**b**) of the MIL-101(Fe,Cu) and C_{60}/MIL-101(Fe,Cu)

and the degradation rate of MB was 99.2% after 50 min of illumination. In order to test the photo-Fenton degradation ability of MB by C_{60}/MIL-101 (Fe, Cu) materials in different systems, the experimental results of test (b, c, f) were obtained. According to the analysis of test b, the degradation efficiency of C_{60}/MIL-101(Fe,Cu) reached 87.4% in a single Fenton system with only H_2O_2 added. According to the analysis of test c, the efficiency of C_{60}/MIL-101(Fe,Cu) reached 87.5% in a single photocatalytic system. The composites showed good catalytic performance in either fenton or photocatalytic systems. The two systems were combined to form a heterogeneous photo-Fenton catalytic system (test f), and the degradation efficiency of the composite system was improved by about 11.8% compared with the original single system. These results indicated that C_{60}/MIL-101(Fe,Cu) had a remarkable effect on the degradation of dye wastewater in the photo-Fenton system.
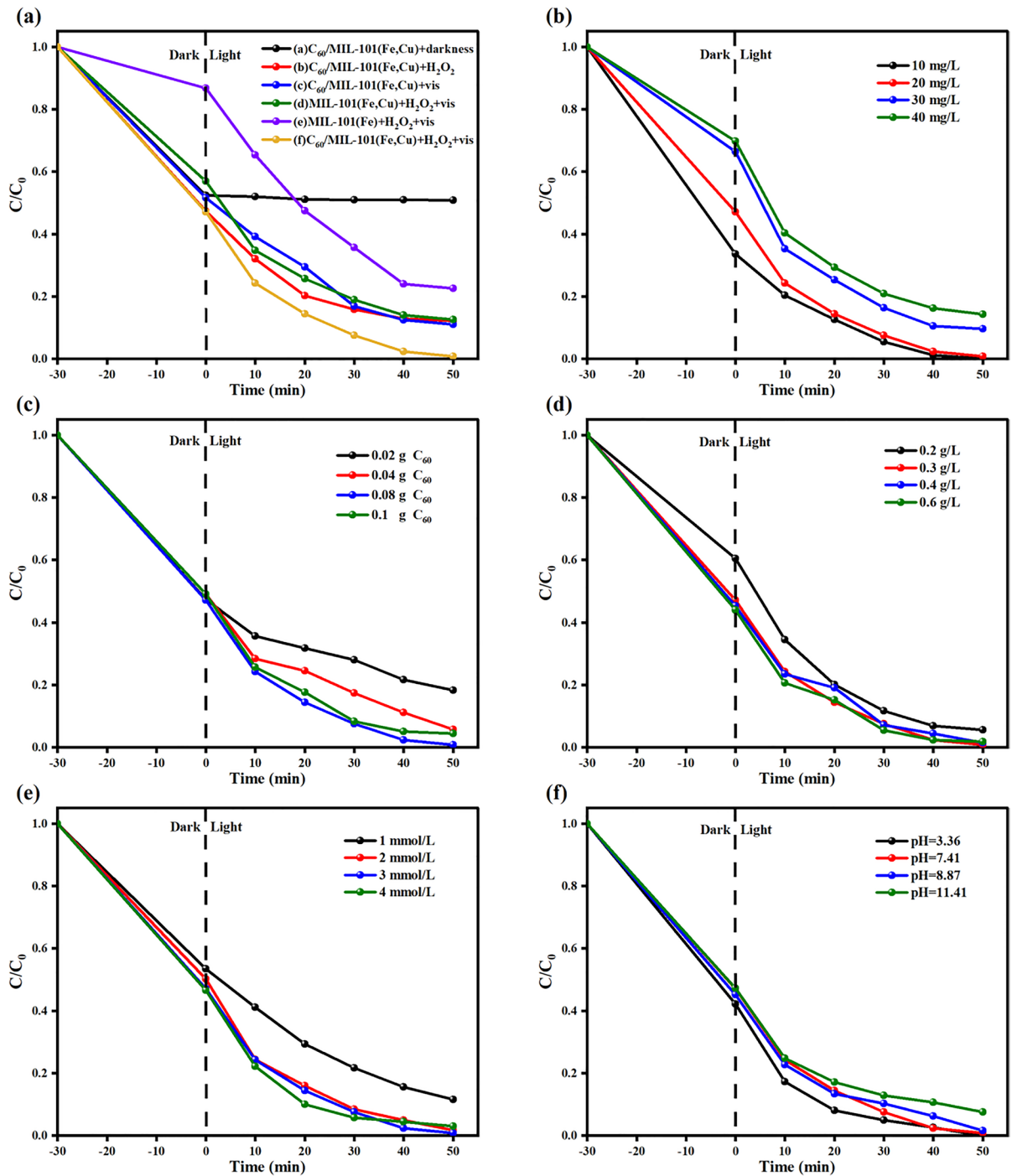
3.6.2 Effect of Initial Concentration

The initial concentration had a significant effect on the MB degradation performance. Figure 7b showed that the increase in MB concentration had an unfavourable effect on MB removal. At an initial concentration of 10 mg/L, MB was completely removed (100%) at 80 min. When the amount of MB was increased to 20 mg/L, 30 mg/L and 40 mg/L, the

removal rate decreased to 99.2%, 90.4% and 85.8% within 80 min, respectively. The high concentration of pollutant solution may compete to occupy the catalytic active sites of C_{60}/MIL-101(Fe,Cu), reducing the amount of active substances in the reaction solution, which led to the reduction of the removal rate (Khajeh et al., 2022). The univariate experiments were continued in subsequent experiments with 20 mg/L MB solution.

3.6.3 Effect of Incorporation of C_{60}

The C_{60}/MIL-101(Fe,Cu) catalysts were synthesized with different ratios by doping 0.02 g, 0.04 g, 0.08 g and 0.1 g of C_{60}, respectively. The photodegradation experiments were carried out by adding 3 mmol/L H_2O_2 under visible light irradiation. As shown in Fig. 7c, the photodegradation efficiency of C_{60}/MIL-101(Fe,Cu) catalyst increased with the increase of the doping ratio, and the degradation efficiency was not significantly improved when the doping ratio was increased to a certain extent. It indicated that the photocatalytic performance of C_{60}/MIL-101(Fe,Cu) composites was enhanced by the addition of C_{60}. Due to the expensive price of C_{60}, the optimum doping ratio of 0.08 g fullerene was used in the subsequent experiments considering the economy.

Fig. 7 Effect of different catalytic systems (**a**), initial concentration (**b**), incorporation of C_{60} (**c**), catalyst dosage (**d**), H_2O_2 dosage (**e**), initial pH (**f**)

3.6.4 Effect of Catalyst Dosage

In order to investigate the effect of catalyst dosage on the degradation performance, 0.2 g/L, 0.3 g/L, 0.4 g/L and 0.6 g/L of C_{60}/MIL-101(Fe,Cu) catalysts were injected, respectively. The photocatalytic experiment was carried out on 50 mL 20 mg/L MB solution under visible light irradiation. As shown in Fig. 7d, the degradation of C_{60}/MIL-101(Fe,Cu) gradually increased from 94.5% to 99.4%. This was attributed to the increase of the active sites on the catalyst surface with the increase of catalytic dosage, which improves the absorption performance and promotes the generation of hydroxyl radicals (Roy et al., 2023). Considering the degradation efficiency and economy, 0.3 g/L was used as the optimal catalytic dosage for subsequent experiments.

3.6.5 Effect of H_2O_2 Dosage

The effect of the addition of H_2O_2 on the degradation performance of C_{60}/MIL-101(Fe,Cu) was investigated, and the photocatalytic reaction experiments were carried out by adding 1–4 mmol/L H_2O_2, respectively. As shown in Fig. 7e, the efficiency of photo-degradation gradually increased with the increase of H_2O_2 dosage. This was because more ·OH was produced to promote pollutant degradation with the increase of H_2O_2 dosage. However, too high concentration of hydrogen peroxide will inhibit the degradation efficiency. The possible reason was that high concentration of hydrogen peroxide (4 mmol/L) becomed the quenching agent of ·OH during the degradation process. According to the actual situation, 3 mmol/L hydrogen peroxide was the most suitable experimental condition.

3.6.6 Effect of Initial pH

The initial pH of the reaction system was adjusted to 3.36, 7.41 (irregular), 8.87 and 11.41 respectively with dilute hydrochloric acid, and the photo-Fenton degradation experiment was carried out under visible light irradiation. As shown in Fig. 7f, the photodegradation effect of the composite catalyst was the highest when the pH was weakly alkaline (7.41). It can also be seen from the experiment that the catalyst C_{60}/MIL-101(Fe,Cu) had a good removal efficiency for MB at 3.36–11.41, which was attributed to the electronegativity of the catalyst surface and the presence of oxygen-containing functional groups. The C_{60}/MIL-101(Fe,Cu) photocatalyst had a wide range of pH applicability to meet the requirements of national environmental water samples (pH = 6–9).
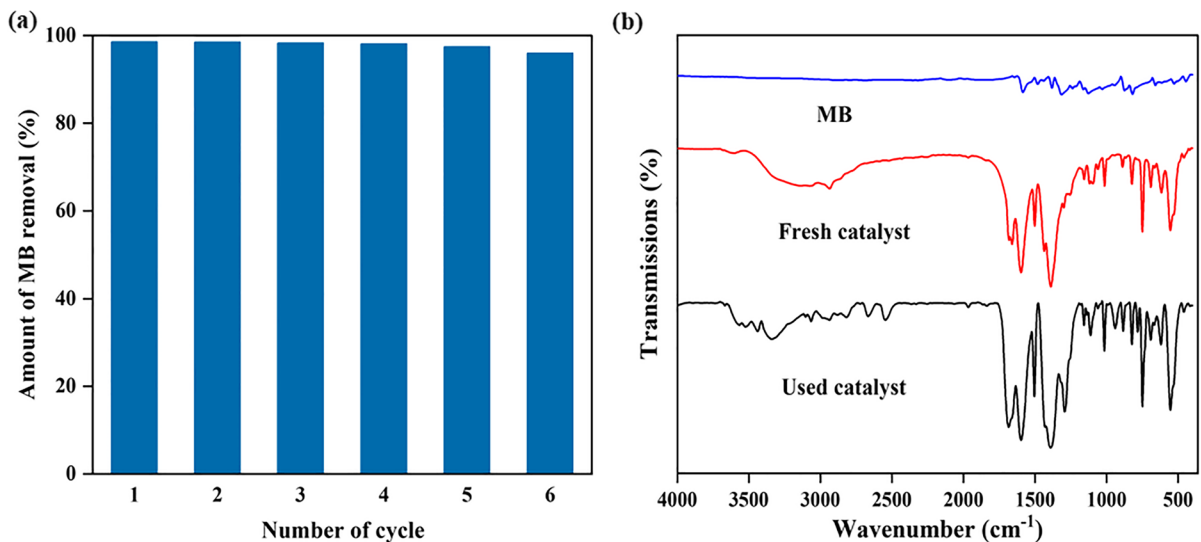
Fig. 8 Recycle test for MB degradation (**a**), FT-IR spectra of MB, fresh and used catalyst (**b**)

3.7 Reusability of C_{60}/MIL-101(Fe,Cu)

To investigate the stability of C_{60}/MIL-101(Fe,Cu) material, cyclic degradation experiments were carried out. After six cycles, the experimental results of MB degradation rate were shown in Fig. 8a, and the catalytic degradation rate of MB decreased from 99.2% to 95.9%, still maintaining a high degradation efficiency of MB, which indicates that the material has excellent recyclability (Moalej et al., 2023). At the same time, the FT-IR characterization of C_{60}/MIL-101(Fe,Cu) material after cycles was carried out (Fig. 8b). The FT-IR characteristic diffraction peaks of the material before and after the reaction were consistent, indicating that the functional groups did not change significantly and the material had high stability. These experimental results showed that C_{60}/MIL-101(Fe,Cu) had high cyclic catalytic capacity and good stability.

The thermogravimetric analysis (TG) and derivative thermogravimetry (DTG) curves in Fig. 9 showed that the weight loss ratio and weight loss rate of MIL-101(Fe,Cu) and C_{60}/MIL-101(Fe,Cu) materials change with temperature. Among them, between 350 ℃ and 420 ℃, the weight of the two materials droped sharply, which may be due to the high temperature carbonization of the organic ligand (H_2BDC) in the MOF, which caused the organic skeleton to collapse. The process of pyrolysis of the material at high temperature revealed

the weight change of the composite, but C_{60}/MIL-101(Fe,Cu) still showed good thermal stability.

## 3.8 Possible Catalytic Mechanism

Figure 10a showed the capture experiment and the role of various active radicals in the degradation of MB. Active radical trapping experiments were mainly the addition of trapping agents, which were able to react with free radicals, thereby reducing or eliminating the number of Active radicals. This process usually involved the transfer of e^- or hydrogen atoms between the free radical and the trapping agent. The degradation rate of MB decreased from 99.2% to 44.79% after adding IPA (·OH trapping agent) for 80 min. When $CHCl_3$ (·O_2^- trapping agent) was added, the degradation rate of MB was reduced to 53.6%. With the addition of EDTA-2Na (h^+ trapping agent), the degradation rate of MB decreased to 76.92%. The addition of L-Histidine ($^1O_2$ trapping agent) had no significant effect on MB degradation. This indicated that the active species that played a major role in the degradation experiment were ·OH, ·O_2^- and h^+ (Alikarami et al., 2023; Angkaew et al., 2021). Figure 10b further verified the free radicals in the catalytic system through EPR testing technology, and the characteristic signal peaks of ·OH and ·O_2^- can be detected under the combined action of visible light and hydrogen peroxide. According to the above experimental results, ·OH and ·O_2^- were the main active free radicals for
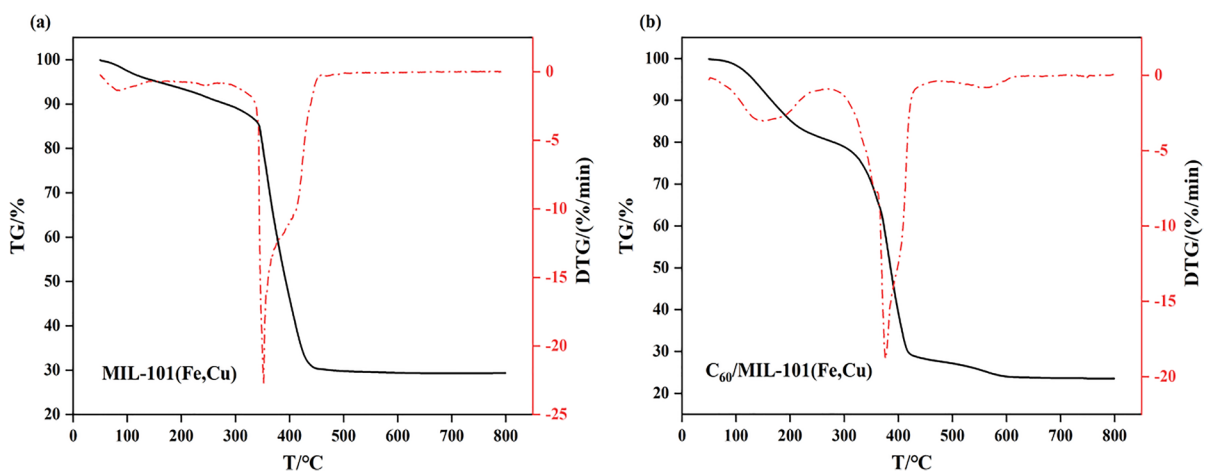
Fig. 9 TG and DTG curves of MIL-101(Fe,Cu) (**a**) and C_{60}/MIL-101(Fe,Cu) (**b**)
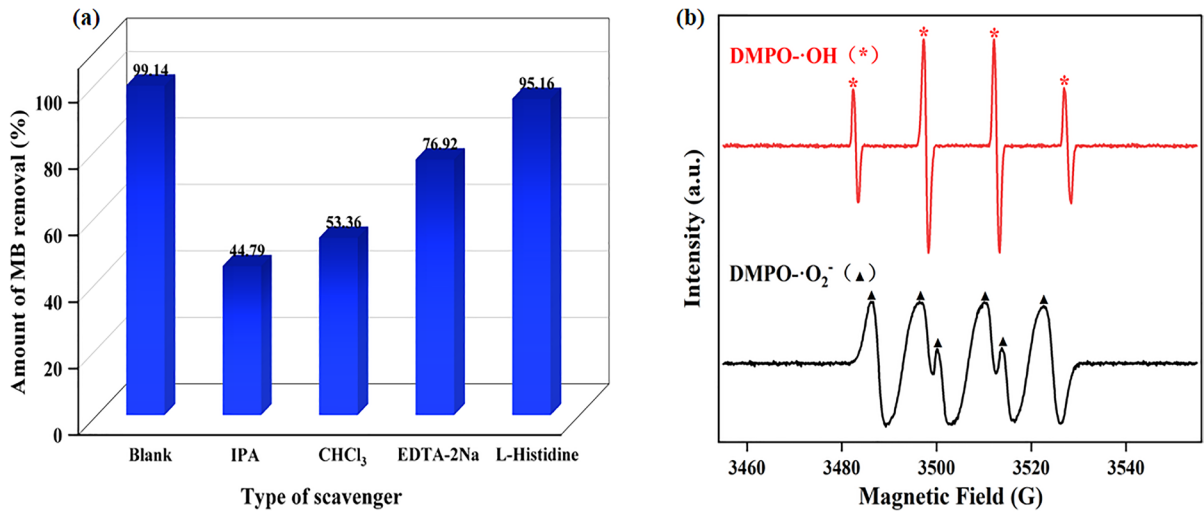
Fig. 10 Effects of radical scavengers for MB degradation in the photo-Fenton system (**a**), EPR spectra detected in photo-Fenton and Fenton systems for DMPO-·OH and DMPO-·O$_2^-$ (**b**)
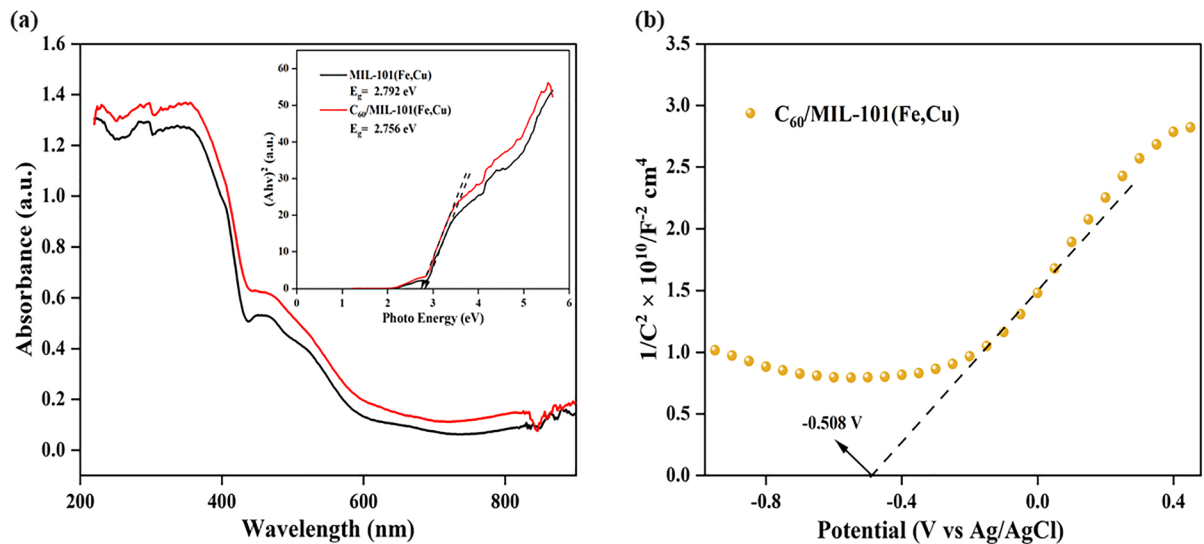
Fig. 11 UV–vis DRS spectra of MIL-101(Fe,Cu) and C$_{60}$/MIL-101(Fe,Cu) (**a**), Mott-Schottky plot of C$_{60}$/MIL-101(Fe,Cu)

photocatalytic degradation of MB in the C$_{60}$/MIL-101(Fe,Cu) photo-Fenton degradation system, and h$^+$ also played an important role in the degradation process.

The light absorption degree of the material can be understood through the characterization of UV–vis diffuse reflection spectrum. As shown in Fig. 11a, C60/MIL-101(Fe,Cu) exhibited better absorption in the visible region than MIL-101(Fe,Cu). The optical band gap energy (E$_g$) of materials was calculated on the basis of Kubelka–Munk equation as:

$$\alpha h v = A\left(h v - E_g\right)^{n/2} \tag{2}$$

where α, h, v and A represent absorption coefficient, Planck constant, light frequency and proportionality constant, respectively. The E$_g$ values of

MIL-101(Fe,Cu) and C_{60}/MIL-101(Fe,Cu) were 2.792 eV and 2.756 eV respectively.

To determine the semiconductor type and photo-Fenton mechanism, the mott-Schottky plot of C_{60}/MIL-101(Fe,Cu) was measured electrochemically. The positive slope of the Mott-Schottky curve (Fig. 11b) indicated that the material was an n-type semiconductor. The flat-band potential of an n-type semiconductor was about 0.097 eV higher than the conduction-band potential (E_{CB}). Therefore, the E_{CB} values of C_{60}/MIL-101(Fe,Cu) was -0.411 eV (versus. NHE). Because $E_{VB} = E_g + E_{CB}$ ($E_g = 2.756$ eV), the valence band (E_{VB}) potentials of C_{60}/MIL-101(Fe,Cu) was 2.345 eV (versus. NHE) (Yang et al., 2020).

According to UV–vis diffuse reflection spectrum and electrochemical calculation analysis, the reaction mechanism as follows was proposed (Fig. 12). The C_{60}/MIL-101(Fe,Cu) material absorbed light energy and generated photogenerated electron–hole pairs. Since the E_{VB} (2.345 eV) of C_{60}/MIL-101(Fe,Cu) material was positive than $E(H_2O/\cdot OH) = 2.27$ eV (vs NHE), h^+ can oxidize the H_2O to $\cdot OH$. Meanwhile, C_{60}/MIL-101(Fe,Cu) had a more negative E_{CB} (-0.411 eV) than $E(O_2/\cdot O_2^-) = -0.33$ eV (vs NHE). Therefore, the electrons were able to reduce the O_2 adsorbed on its surface to $\cdot O_2^-$. At the same time, in

the process of photocatalysis, Fe^{3+} (Cu^{2+}) on the surface of C_{60}/MIL-101(Fe,Cu) absorbed electrons and generates Fe^{2+} (Cu^+) ions after the electron transition to the conduction band. The generated Fe^{2+} (Cu^+) ions can react with hydrogen peroxide to form $\cdot OH$, and Fe^{2+} (Cu^+) was oxidized to Fe^{3+} (Cu^{2+}), and the Fe^{3+}/Fe^{2+} (Cu^{2+}/Cu^+) cycle can be achieved. Therefore, in the degradation process, the photocatalytic reaction and the Fenton-like reaction would occur at the same time to produce a large amount of $\cdot OH$ to improve the photocatalytic efficiency. Thus, these active species can further directly oxidize MB to CO_2, H_2O, and other small molecule inorganic substances (Duan et al., 2022; Nadeem et al., 2022).

4 Conclusions

In this study, C_{60}/MIL-101(Fe,Cu) was prepared by one-step solvothermal method. Compared with MIL-101(Fe,Cu) and MIL-101(Fe,Cu), C_{60}/MIL-101(Fe,Cu) had stronger adsorption, catalytic, electrochemical and degradation properties. The single factor experiment on MB degradation of composite materials was carried out. The experimental results showed that the material had significant degradation

Fig. 12 Possible photo-Fenton degradation mechanism upon the C_{60}/MIL-101(Fe,Cu)
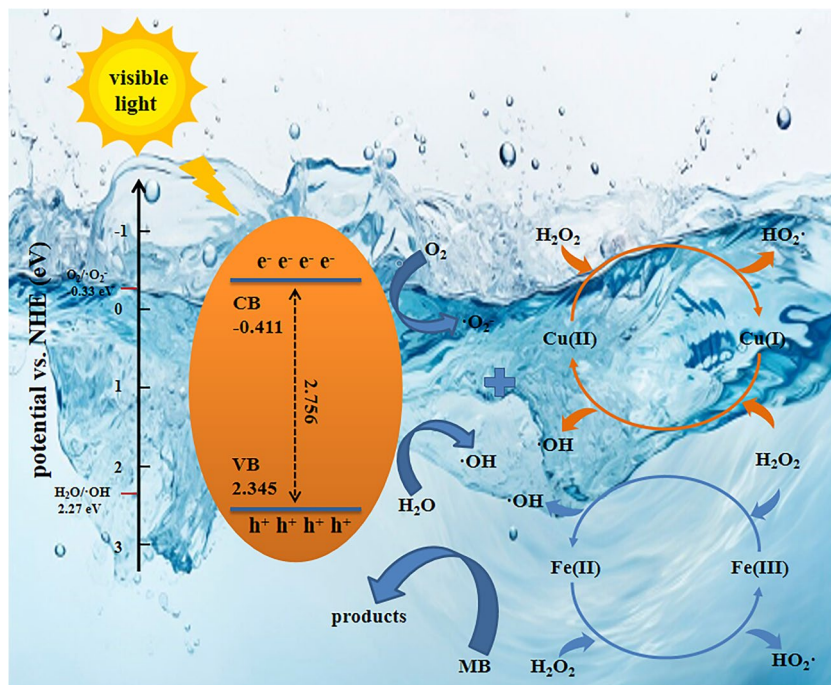
ability under different systems, different initial concentration of pollutants, different incorporation of C_{60}, different catalytic dosage, different H_2O_2 dosage and different initial ph. Through quenching experiment and EPR characterization, we found that $\cdot OH$ and $\cdot O_2^-$ were active species that play a major role in oxidation. At the same time, after 6 cycles of experiments, the degradation efficiency of MB was not significantly reduced. By doping C_{60} and Cu in MIL-101(Fe), the REDOX cycle of Fe^{3+}/Fe^{2+} was greatly promoted. This study was expected to provide new ideas for promoting Fe^{3+}/Fe^{2+} cycling, and enabled C_{60}/MIL-101(Fe,Cu) to be applied to large-scale industrial wastewater treatment in the future.

Author contributions ZZ and YJ are co-authors of this article. ZZ and YJ conceptualized the project methodology, wrote the original draft, revised the manuscript, and supervised the investigation. XY, RL and MY conducted literature research and data collection. YW, ML and CZ co-wrote and revised the manuscript.

Data Availability The authors declare that all data supporting the fndings and materials of this study are available within the paper.

Declarations

Competing interest The authors declare that they have no known competing financial interests or personal relationships that could have appeared to influence the work reported in the submitted manuscript.

References

Aliannezhadi, M., Abbaspoor, M., Tehrani, F. S., & Jamali, M. (2023). High photocatalytic WO3 nanoparticles synthesized using Sol-gel method at different stirring times. *Optical and Quantum Electronics, 55*, 18.

Alikarami, S., Soltanizadeh, A., & Rashchi, F. (2023). Enhancing decomposition of rhodamine (RhB) and methylene blue (MB) using CdS decorated with Ag or Ru driven by visible radiation. *Environmental Science and Pollution Research, 30*, 62847–62866.

Angkaew, A., Chokejaroenrat, C., Sakulthaew, C., Mao, J., Watcharatharapong, T., Watcharenwong, A., Imman, S., Suriyachai, N., & Kreetachat, T. (2021). Two facile synthesis routes

for magnetic recoverable MnFe2O4/g-C3N4 nanocomposites to enhance visible light photo-Fenton activity for methylene blue degradation. *Journal of Environmental Chemical Engineering, 9*, 14.

Ansari, S. N., Kumar, P., Gupta, A. K., Mathur, P., & Mobin, S. M. (2019). Catalytic CO2 Fixation over a Robust Lactam-Functionalized Cu(II) Metal Organic Framework. *Inorganic Chemistry, 58*, 9723–9732.

Cen, S. H., Lv, X. G., Jiang, Y. L., Fakhri, A., & Gupta, V. K. (2020). Synthesis and structure of iron-copper/hollow magnetic/metal-organic framework/coordination sites in a heterogeneous catalyst for a Fenton-based reaction. *Catalysis Science & Technology, 10*, 6687–6693.

Chavan, R., Bhat, N., Parit, S., Narasimharao, K., Devan, R. S., Patil, R. B., Karade, V. C., Pawar, N. V., Kim, J. H., Jadhav, J. P., & Chougale, A. D. (2023). Development of magnetically recyclable nanocatalyst for enhanced Fenton and photo-Fenton degradation of MB and Cr(VI) photoreduction. *Materials Chemistry and Physics, 293*, 11.

Chen, Y., Shi, Y. H., Wan, D. J., Zhao, J. H., He, Q. C., & Liu, Y. D. (2022). Synergistic adsorption and advanced oxidation activated by persulfate for degradation of tetracycline hydrochloride using iron-modified spent bleaching earth carbon. *Environmental Science and Pollution Research, 29*, 24704–24715.

Chen, Y. H., Liu, X. Z., Guo, S. L., Cao, J., Zhou, J., Zuo, J. L., & Bai, L. J. (2019). A sandwich-type electrochemical aptasensor for Mycobacterium tuberculosis MPT64 antigen detection using C60NPs decorated N-CNTs/GO nanocomposite coupled with conductive PEI-functionalized metal-organic framework. *Biomaterials, 216*, 10.

Dhankhar, A., Rai, R. K., Tyagi, D., Yao, X., & Singh, S. K. (2016). Synergistic Catalysis with MIL-101: Stabilized Highly Active Bimetallic NiPd and CuPd Alloy Nanoparticle Catalysts for C-C Coupling Reactions. *ChemistrySelect, 1*, 3223–3227.

Ding, L., Zeng, M., Wang, H., & Jiang, X. B. (2021). Synthesis of MIL-101-derived bimetal-organic framework and applications for lithium-ion batteries. *J. Mater. Sci.-Mater. Electron, 32*, 1778–1786.

Du, C. Y., Zhang, Y., Zhang, Z., Zhou, L., Yu, G. L., Wen, X. F., Chi, T. Y., Wang, G. L., Su, Y. H., Deng, F. F., Lv, Y. C., & Zhu, H. (2022). Fe-based metal organic frameworks (Fe-MOFs) for organic pollutants removal via photo-Fenton: A review. *Chemical Engineering Journal, 431*, 18.

Duan, M. J., Guan, Z. Y., Ma, Y. W., Wan, J. Q., Wang, Y., & Qu, Y. F. (2018). A novel catalyst of MIL-101(Fe) doped with Co and Cu as persulfate activator: Synthesis, characterization, and catalytic performance. *Chemical Papers, 72*, 235–250.

Duan, Y. Z., Li, J., Jia, D. M., Yao, H. B., Shang, X. L., & Li, C. H. (2022). One-step synthesis of Mg-doped g-C3N4 nanosheets for efficient photo-Fenton-like catalysis. *Diamond and Related Materials, 129*, 12.

Feizpoor, S., Habibi-Yangjeh, A., & Luque, R. (2023). Preparation of TiO2/Fe-MOF n-n heterojunction photocatalysts for visible-light degradation of tetracycline hydrochloride. *Chemosphere, 336*, 139101.

Feng, Z. M., Yang, J. W., Zhu, L. Y., & Sun, T. (2023). Bromine functionalized Fe/Cu bimetallic MOFs for accelerating Fe(III)/Fe (II) cycle and efficient degradation of

phenol in Fenton-like system. *Colloids and Surfaces A: Physicochemical and Engineering Aspects, 658*, 8.

Granados-Tavera, K., Montenegro-Pohlhammer, N., & Cárdenas-Jirón, G. (2023). 'Photoconductive metal-organic frameworks based on 10,20-meso-substi-tuted Zn-porphyrin and fullerene C_{60}. *Surfaces and Interfaces, 40*, 11.

Gu, D. X., Liu, Y., Zhu, H. Y., Gan, Y., Zhang, B., Yang, W. T., & Hao, J. Y. (2022). Magnetic porphyrin-based metal organic gel for rapid RhB removal and enhanced antibacterial activity by heterogeneous Photo-Fenton reaction under visible light. *Chemosphere, 303*, 11.

Deng, L. L., Yin, D. G., Khaing, K. K., Xiao, S. T., Li, L. Q., Guo, X. D., Wang, J., & Zhang, Y. (2020). Facile boosting sunlight-driven photocatalytic performance of metal-organic-framework through coupling with Ag_2S nanoparticles. *New Journal of Chemistry, 44*, 12568–12578.

Guo, Y., Feng, C., Qiao, S. S., Wang, S. X., Chen, T. X., Zhang, L., Zhao, Y. S., & Wang, J. D. (2020). Magnetic Fe_3O_4-encapsulated VAN@MIL-101(Fe) with mixed-valence sites and mesoporous structures as efficient bifunctional water splitting photocatalysts. *Nanoscale, 12*, 12551–12560.

Hui, K. C., Ang, W. L., Yahya, W. Z. N., & Sambudi, N. S. (2022). Effects of nitrogen/bismuth-doping on the photocatalyst composite of carbon dots/titanium dioxide nanoparticles (CDs/TNP) for enhanced visible light-driven removal of diclofenac. *Chemosphere, 290*, 12.

Hussain, A., Ali, N., Ali, S. S., Hou, J. H., Aslam, I., Naeem, H., Boota, M., Ul-Hussan, M., Yin, J., & Wang, X. Z. (2022). Diverse morphological study for nonmetal-doped g-C_3N_4 composites with narrow bandgap for improved photocatalytic activity. *Research on Chemical Intermediates, 48*, 2857–2870.

Khajeh, M., Oveisi, A. R., Barkhordar, A., Rakhshanipour, M., & Sargazi-Avval, H. (2022). 'Ternary NiCuZr layered double hydroxide@MIL-101 (Fe)-NH_2 metal-organic framework for photocatalytic degradation of methylene blue. *Journal of Nanostructure in Chemistry, 12*, 105–115.

Khosravi, F., Gholinejad, M., Sansano, J. M., & Luque, R. (2022). Bimetallic Fe-Cu metal organic frameworks for room temperature catalysis. *Applied Organometallic Chemistry, 36*, 22.

Li, X. H., Guo, W. L., Liu, Z. H., Wang, R. Q., & Liu, H. (2017). Quinone-modified NH_2-MIL-101(Fe) composite as a redox mediator for improved degradation of bisphenol A. *Journal of Hazardous Materials, 324*, 665–672.

Li, Z. S., Tang, X. K., Huang, G. H., Luo, X. P., He, D. S., Peng, Q., Huang, J., Ao, M. L., & Liu, K. (2020). 'Bismuth MOFs based hierarchical Co_3O_4-Bi_2O_3 composite: An efficient heterogeneous peroxymonosulfate activator for azo dyes degradation. *Separation and Purification Technology, 242*, 11.

Li, Z. S., Tang, X. K., Liu, K., Huang, J., Peng, Q., Ao, M. L., & Huang, Z. G. (2018). Fabrication of novel sandwich nanocomposite as an efficient and regenerable adsorbent for methylene blue and Pb (II) ion removal. *Journal of Environmental Management, 218*, 363–373.

Liang, H., Liu, R. P., An, X. Q., Hu, C. Z., Zhang, X. W., & Liu, H. J. (2021). Bimetal-organic frameworks with coordinatively unsaturated metal sites for highly efficient

Fenton-like catalysis. *Chemical Engineering Journal, 414*, 11.

Lin, J. L., Hu, H., Gao, N. Y., Ye, J. S., Chen, Y. J., & Ou, H. S. (2020). Fabrication of GO@MIL-101(Fe) for enhanced visible-light photocatalysis degradation of organophosphorus contaminant. *Journal of Water Process Engineering, 33*, 9.

Zhu, D. Y., Huang, Z. J., Wang, H. Y., Lu, Q. J., Ruan, G. H., Zhao, C. X., & Du, F. Y. (2022). Sustainable and reusable electrospun g-C_3N_5/MIL-101(Fe)/poly(acrylonitrile-co-maleic acid)nanofibers for photocatalytic degradation of emerging pharmaceutical pollutants. *New Journal of Chemistry, 46*, 11840.

Lin, H. X., Wu, J. M., Zhou, F., Zhao, X. L., Lu, P. F., Sun, G. H., Song, Y. H., Li, Y. Y., Liu, X. Y., & Dai, H. X. (2023). Graphitic carbon nitride-based photocatalysts in the applications of environmental catalysis. *Journal of Environmental Sciences, 124*, 570–590.

Lu, L. H., Shu, Q. L., Zhang, G. R., Zhang, Q., Du, P., & Zhu, X. D. (2022). Mechanism in chlorine-enhanced Pd catalyst for H_2O_2 in situ synthesis in electro-Fenton system. *AIChE Journal, 68*, 16.

Lu, X. Y., Che, Q. M., Niu, X. K., Zhang, Y. L., Chen, Y. E., Han, Q., Li, M. Q., Wang, S., & Lan, J. H. (2023). Catalytic Degradation of Triphenylmethane Dyes with an Iron Porphyrin Complex as a Cytochrome P450 Model. *Molecules, 28*, 12.

Moalej, N. S., Sheibani, S. & Mokmeli, M. (2023). Ternary Z-scheme NiO/CdO/Co_3O_4 nanocomposite powder with enhanced photocatalytic activity under visible light irradiation. *J. Mater. Sci.-Mater. Electron, 34*, 16.

Nadeem, N., Yaseen, M., Rehan, Z. A., Zahid, M., Shakoor, R. A., Jilani, A., Iqbal, J., Rasul, S., & Shahid, I. (2022). Coal fly ash supported $CoFe_2O_4$ nanocomposites: Synergetic Fenton-like and photocatalytic degradation of methylene blue. *Environmental Research, 206*, 13.

Pestana, C. J., Hui, J. N., Camacho-Munoz, D., Edwards, C., Robertson, P. K. J., Irvine, J. T. S., & Lawton, L. A. (2023). Solar-driven semi-conductor photocatalytic water treatment (TiO2, g-C3N4, and TiO2+g-C_3N_4) of cyanotoxins: Proof-of-concept study with microcystin-LR. *Chemosphere, 310*, 10.

Roy, S., Darabdhara, J., & Ahmaruzzaman, M. (2023). ZnO-based Cu metal-organic framework (MOF) nanocomposite for boosting and tuning the photocatalytic degradation performance. *Environmental Science and Pollution Research, 30*, 95673–95691.

Shah, A. H., Abideen, Z. U., Maqsood, S., Rashid, F., Ullah, R., Rehman, A. U., Dildar, M., Ahmad, M., Ullah, K., Rafi, M. N., & Teng, F. (2023). Porous Cu-based metal organic framework (Cu-MOF) for highly selective adsorption of organic pollutants. *Journal of Solid State Chemistry, 322*, 10.

Shaheen, S., Saeed, Z., Ahmad, A., Pervaiz, M., Younas, U., Khan, R. R. M., Luque, R., & Rajendran, S. (2023). Green synthesis of graphene-based metal nanocomposite for electro and photocatalytic activity; recent advancement and future prospective. *Chemosphere, 311*, 17.

Sharma, A., Tahir, M., Ahamad, T., Kumar, N., Sharma, S., Kumari, M., Khan, M. A. M., Takhur, S., & Raizada, P. (2023). Improved charge transfer and enhanced visible

light photocatalytic activity of Bi_2O_3@Fe-MOF for degradation of Rhodamine B and Triclopyr. *Journal of King Saud University, 35*, 9.

Tao, X. M., Yuan, X. J., & Huang, L. (2021). Effects of Fe(II)/Fe(III) of Fe-MOFs on catalytic performance in plasma/Fenton-like system. *Colloids and Surfaces A: Physicochemical and Engineering Aspects, 610*, 8.

Tayeb, A. M., Mostafa, N. A., Barakat, N. A. M., Mohamed, S. N., & Monazie, A. M. (2023). Optimisation study for photocatalytic degradation of methylene blue using TiO_2 supported on Agar-Agar and doped with silver. *International Journal of Environmental Analytical Chemistry, 103*, 7152–7167.

Wan, Y. J., Wan, J. Q., Ma, Y. W., Wang, Y., & Luo, T. (2020). Sustainable synthesis of modulated Fe-MOFs with enhanced catalyst performance for persulfate to degrade organic pollutants. *Science of the Total Environment, 701*, 12.

Watariguchi, S., Ueno, Y., Fujimori, M., & Hinoue, T. (2014). A New-Type Photovoltaic Cell Using Photochemical Reaction of Fullerene. *Electrochemistry, 82*, 736–742.

Wu, Y., Liu, Z. N., Bakhtari, M. F. & Luo, J. N. (2021). Preparation of GO/MIL-101(Fe,cu) composite and its adsorption mechanisms for phosphate in aqueous solution (May, https://doi.org/10.1007/s11356-021-14206-9, 2021). *Environ. Sci. Pollut. Res, 28*, 51404–51404.

Xiong, P., Zhang, H., Li, G. L., Liao, C. Y., & Jiang, G. B. (2021). Adsorption removal of ibuprofen and naproxen from aqueous solution with Cu-doped Mil-101(Fe). *Science of the Total Environment, 797*, 9.

Xu, C. X., Kong, Y. L., Zhang, W. J., Yang, M. D., Wang, K., Chang, L., Chen, W., Huang, G. B., & Zhang, J. (2022). S-scheme 2D/2D $FeTiO_3$/g-C_3N_4 hybrid architectures as visible-light-driven photo-Fenton catalysts for tetracycline hydrochloride degradation. *Separation and Purification Technology, 303*, 12.

Yang, Q. A., Wei, S. Q., Zhang, L. M., & Yang, R. (2020). Ultrasound-assisted synthesis of $BiVO_4$/C-dots/g-C_3N_4 Z-scheme heterojunction photocatalysts for degradation of minocycline hydrochloride and Rhodamine B: Optimization and mechanism investigation. *New Journal of Chemistry, 44*, 17641–17653.

Yang, T. Y., Yu, D. Y., Wang, D., Yang, T., Li, Z. X., Wu, M. H., Petru, M., & Crittenden, J. (2021). Accelerating Fe(III)/Fe(II) cycle via Fe(II) substitution for enhancing Fenton-like performance of Fe-MOFs. *Appl. Catal. B-Environ, 286*, 11.

Zhang, N., Sun, N. R., & Deng, C. H. (2020). A hydrophilic magnetic MOF for the consecutive enrichment of exosomes and exosomal phosphopeptides. *Chemical Communications, 56*, 13999–14002.

Zhang, X., Zhang, W., Ran, L., Wang, X. Y., Zou, B. Z., & Zhou, L. C. (2022). Mechanism and performance evaluation of $FeSe_2$ and MoS_2-loaded carbon fiber sheet as a novel heterogeneous Fenton-like catalyst. *Applied Surface Science, 598*, 15.